PNAS
www.pnas.org

Supplementary Information for

Unraveling materials Berry curvature and Chern numbers from real-time evolution of Bloch states

Dongbin Shin, Shunsuke A. Sato, Hannes Hübener, Umberto De Giovannini, Jeongwoo Kim, Noejung Park and Angel Rubio

Noejung Park and Angel Rubio.
E-mail: noejung@unist.ac.kr and angel.rubio@mpsd.mpg.de

This PDF file includes:

Supplementary text
Figs. S1 to S6
References for SI reference citations

www.pnas.org/cgi/doi/10.1073/pnas.1816904116

Supporting Information Text

Parameters for the ground state DFT and time-integration algorithms

The equilibrium atomic geometry and the ground state electronic structure are obtained by standard density functional theory (DFT) calculation using Octopus and Quantum Espresso package (1–5). To describe the exchange and correlation of electrons, Perdew-Burke-Ernzerhof (PBE)-type generalized gradient approximation functional is employed (6). The nuclei potentials are described by norm-conserving pseudopotentials. The Brillouin zone is integrated using Monkhorst-Pack scheme: the grid of $6 \times 6 \times 6$, $12 \times 12 \times 1$, $20 \times 20 \times 1$, and $9 \times 9 \times 1$ is used for the solid He, Graphene, half-passivated Stanene, and Bismuthane, respectively. To optimize the geometry, the forces on each atom are relaxed within $10^{-5} Ry/Bohr$. To propagate the KS states, we start with the ground state orbitals at $t = 0$, obtained by standard DFT calculation. The wavefunction at $t + \Delta t$ is evolved from that at t with

$$\psi_n\left(t+\Delta t\right) = \exp\left(-i\Delta t \hat{H}[\rho(t)]/\hbar\right)\psi_n\left(t\right) \qquad [1]$$

For the time-dependent Hamiltonian, the external time-dependent potential is added to the Kohn-Sham Hamiltonian constructed as a functional of the density at time t. In Eq. S1, the band index and the Bloch vector are collectively denoted by the subscript n. The evolved charge density $\rho\left(t+\Delta t\right)$ is calculated from the squared sum of the evolved KS wavefunctions: $\rho\left(t+\Delta t\right) = \sum_n \left|\psi_n\left(t+\Delta t\right)\right|^2$, from which the KS Hamiltonian at the next time step $H\left[\rho\left(t+\Delta t\right)\right]$ is again derived. A few algorithms have been tested in the literature to achieve a better consistency between wavefunctions and the Hamiltonian. For example, the consistency of the density at the intermediate step between that of forward evolution from the previous step and that of backward evolution from the next step is a good criterion. Many detailed formalisms regarding this method were published by numerous authors including us (2, 7–9).

Static constant uniform electric field (E-field) is expressed in the velocity gauge as a vector potential through the relation: $\mathbf{E} = \frac{1}{c}\partial\mathbf{A}\left(t\right)/\partial t$. However, throughout our works, to achieve a better adiabatic evolution, the E-field is gradually turned-on during the initial period (τ):

$$A\left(t\right) = \begin{cases} cE_0\chi(t,\tau), & 0 \le t < \tau \\ cE_0\left(t-\tau+\chi(\tau,\tau)\right), & t \ge \tau \end{cases}. \qquad [2]$$

Note that the physical observables were calculated after the turn-on period ($t \ge \tau$) when the E-field strength is constant over time (E_0). The actual shape of $\chi(t,\tau)$ is not essential but needs to be smoothly increasing, for example, $\chi(t,\tau) = t^3/\tau^2 - 0.5t^4/\tau^3$. In the present work, we mainly aimed at materials intrinsic topological property and thus focused on the weak-field regime. In this context, the vector potential is provided purely externally, and the back reaction of the material into the field is not considered. When the material's feedback is substantial, the response of the vector field needs to be considered as suggested by Bertsch et al. (10).

Time profiles of KS states of the artificial He simple cubic solid

Here we show a detailed time profile of the four selected states in the valence band of He solid, which was introduced in Fig. 1 of the main text: Γ, X, Δ, and −Δ. As shown in Fig. 1*A* and Fig. S1*A*, the band gap is so wide ($16.5eV$), and the time profiles of the KS states follow the static energy band very closely: Figure 1*B* and Fig. S1*B* tells that the instantaneous band energy is $\varepsilon\left(t\right) = \varepsilon\left(\mathbf{k}\left(t\right)\right)$ with $\mathbf{k}(t) = \mathbf{k}(0) - et\mathbf{E}/\hbar$. The velocity given by the band energy dispersion, $v\left(\mathbf{k}\right) = \frac{1}{\hbar}\frac{d\varepsilon(\mathbf{k})}{d\mathbf{k}}$, is presented in Fig. S1*C*-*F* for each of the state starting from Γ, X, Δ, and −Δ. Note that, with the given E-field strength, these velocities well produces the oscillation period of $T = 375$fs, which corresponds to the time required for the Bloch state to travel the whole BZ : $(eE/\hbar)T = 2\pi/a_0$.

The electronic structure of the half-hydrogenated Sn

The electronic structure of stanene with the half coverage of the hydrogen passivation, abbreviated as HHS in the main text, is presented in Fig. S2*A*, which is qualitatively the same as the previously reported passivation with halogen atoms (11). Figure S2*B* shows that, when SOC is not counted, the spin-down bands (blue) reveals a gap, while the spin-up bands (red) produce metallic states. Upon the inclusion of realistic SOC, the spin-up bands near the Fermi level are inverted, as presented in Fig. S2*C*. In the time profile, the total energy variation is negligible ($2.4\times10^{-5} eV/fs$) and the system preserved the band structure of the insulator, which proves the adiabatic nature of the time propagation.

The spin current operator used in the present work

For the spin current operator, in the present work, we chose the following form, as represented in the Heisenberg picture,

$$\hat{\mathbf{j}}^{S_Z} = e\frac{d}{dt}\left(\hat{\mathbf{r}}\hat{S}_Z\right) = \frac{e}{2m}\left\{\hat{\boldsymbol{\pi}}, \hat{S}_Z\right\} + \hat{\mathbf{r}}\frac{e}{i\hbar}\left[\hat{S}_Z, \hat{H}\right]. \qquad [3]$$

In the results shown in Fig. 4 of the main text, the effect of second term in Eq. 3 was found to be two orders of magnitude smaller than the first term, thus the very classical form of the spin current operator (the first term of Eq. 3) works efficiently. In this regard, in discussions of the main text, the second term was not explicitly mentioned, though it was fully accounted for in numerical calculations. Note that, since the total spin of the unit-cell is consistently zero, the second term is well defined without gauge ambiguity even for the periodic solid.

QSH phase of half-hydrogen passivated bismuthane

As an additional example of a QSHI, here we consider the inversion symmetry broken bismuthane. When hydrogen atoms are attached only onto the single side of the bismuthene, as shown in Figure S3A, the spinor bands are split and the spin textures are almost lying in the plane, as shown in Figure S3B. The expectation of the spin current operator and charge current operator are calculated with the time-evolving Kohn-Sham spinor states. The obtained spin Hall and charge Hall conductivity, as defined in Eq. 4. And Eq. 6 in the main text, are summarized in Fig. S3C. In the time profile of the system, the total energy variation is negligible ($6.8\times10^{-7}eV/fs$). This result indicates that the time propagation adiabatically preserves the band structure of the insulator.

Effect of a circularly polarized external field on a zig-zag graphene nano-ribbon

To illustrate how our calculation method of physical observable through the TDDFT can include the effect of external time-dependent field, here we calculate the current through a graphene nano-ribbon (GNR) with and without applying a circularly polarized external E-field. Figure S4A depicts the real-time variation of electron density when a constant static bias ($\mathbf{E} = 1.68 \times 10^{-3}\hat{x}V/\text{Å}$) is applied along the ribbon axial direction. As described in the main text, we calculate the time-evolving Kohn-Sham states, and the time-varying density is obtained from the squared sum of the wavefunctions. As the time evolves, the charge accumulates on both edges, depleting the central region of the ribbon, which can be attributed to the valley-Hall nature of the ribbon (12). However, the system preserves the overall time-reversal symmetry, and the ribbon does not accumulate any charge in the transversal direction, and thus any Hall voltage.

The effect of particularly selected external drivers, so as to dynamically break the time-reversal symmetry of the system, has attracted many recent studies (13, 14, 16–19, 23–27). In this perspective, we apply a circularly polarized time-dependent E-field, as an externally-driven time-reversal breaking mechanism. In this computation, the field of $\mathbf{E} = 6.7 \times 10^{-4}(\hat{x} + i\hat{y})e^{-i\omega t}V/\text{Å}$, with $\omega = 1$eV, is added to the static bias, and the current along the graphene nano-ribbon is calculated. Remarkably, the two edges (L and R) now lose the symmetry, and the system develops an overall charge Hall effect across the ribbon width (13). This can be conceived as a real-time manifestation of an effective time-reversal breaking by a circularly polarized external field. T. Oka and H. Aoki suggested a model for photo-Hall effect in graphene (13, 14). Our *ab initio* simulation explicitly proves the concept of time-reversal breaking by a circularly polarized light, which results in the photo-induced charge Hall current. The present concept can be developed as a theoretical framework to unambiguously address topological features of driven states of matter that can be directly linked to experimental observables.

An extension to 3D topological insulator

Our method of dynamical sweeping the Brillouin zone (BZ) can be straight forwardly applied to 3D systems. The anomalous velocity ($\vec{v} = -\frac{e}{\hbar}\vec{E} \times \vec{\Omega}$) can be calculated from the dynamical Bloch states, which can be integrated over the surface of the BZ. However, beyond a mere identification of a non-zero Chern number, the more important and the more relevant question would be whether this dynamical approach can be utilized to discriminate the strong 3D TI from the weak one. In this perspective, the descriptions given in J.E. Moore (2013) and others are noteworthy(28, 29). The 'time-reversal plane' in the 3D BZ, such as $(k_x, k_y, k_z = 0)$ and $(k_x, k_y, k_z = \vec{b}_3/2)$, includes all the time-reversal partners within the plane. Thus the plane constitutes the periodic BZ torus in the same manner as the 2D quantum spin-Hall plane. Our dynamical approach can be used in the calculation of the spin Hall conductivity of these time-reversal planes, which can indicate unambiguously whether the 3D TI comprises a strong TI or a weak one.

As a prototypical example of a weak TI, one might imagine stacked layers of 2D quantum spin Hall insulators coupled through weak interlayer interaction. The quantum spin-Hall conductivity for the quasi 2D system of (k_x, k_y), that can be calculated in the same way as in the main text (Figure 4), should result in the same quantum value irrespective of k_z. Hence, the two time-reversal plane $(k_x, k_y, k_z = 0)$ and $(k_x, k_y, k_z = \vec{b}_3/2)$ produces the same quantum of the spin-Hall conductivity, indicative of the 'weakness' of the topology of the 3D bands. For the case of strong TI, the spin-Hall conductivity from these two time-reversal planes would results in a different quantum value, in the same manner as the product of four Z_2 invariants in each of the plane(30). On the other hand, this feature can be explained with the distributions of the spin-Berry curvature (defined below). As schematically illustrated in the Fig. S6, for a case of strong TI, the spin-Berry curvature is localized near the Γ point, thus the spin-Hall conductivity in the plane of $(k_x, k_y, k_z = \vec{b}_3/2)$ vanishes.

Our main focus in the present work is to prove that the expectation value of physical observables (such as the spin current operators $\hat{\vec{j}}_{S_z} = \hat{S}_z\hat{\vec{v}}$) reveals the topological quality of the 2D materials, irrespective of whether the spin is well preserved or not. To the best of our knowledge, all the well-known examples of 3D strong TI are derived from a rather big unit-cell. In this section, we would only like to describe how the dynamical calculation of the spin Berry curvature points to the signature of the strong nature of the 3D TI.

As an example of 3D strong TI, here we employed Bi_2Se_3 whose atomic geometry, rhombohedral unit-cell, and the BZ are depicted in Fig. S6(A) and S6(B). The band structure near the TRIM point of the 3D Brillouin zone is well established, in which the band inversion occurs only near the Γ point (20). The band structures near the Γ point with (black) and without (red) the spin-orbit coupling (SOC) are presented in Fig. S6(c). In this case of 3D, the spin current would constitute a second-rank tensor $\langle\psi|\,\hat{\vec{S}} \otimes \hat{\vec{v}}\,|\psi\rangle$, and the spin Berry curvature can be defined in analogy to the anomalous velocity: $\sum_\alpha \langle\psi_\alpha|\,\hat{S}_n\hat{\vec{v}}\,|\psi_\alpha\rangle = -\frac{e}{\hbar}\vec{E} \times \vec{\Omega}_n$.

For example, when the external E-field is applied along the z-direction, a diagonal component of the spin Berry curvature tensor can be written as $\Omega_{x,x} = -\frac{\hbar}{eE_z}\sum_{\alpha}^{occ}\langle\psi_\alpha|\,\hat{S}_n\hat{\vec{v}}\,|\psi_\alpha\rangle$. To investigate the distribution of the spin Berry curvature, we calculated the $\Omega_{x,x}$ along the line of $(k_x = 0, k_y = 0, k_z(t))$, as shown in Fig. S6($D$). This result clearly indicates that the spin Berry curvature is sharply concentrated near the band-inverted region (near the Γ point). A full calculation of the quantum spin-Hall aspects of these two time-reversal planes would produce a different quantum of spin-Hall conductivity, indicative of the 3D strong TI of Bi_2Se_3: the plane $(k_x, k_y, k_z = \vec{b}_3/2)$ and $(k_x, k_y, k_z = 0)$ would result in vanishing and finite spin-Hall conductivity, respectively.

Unitary rotation property in expectation value

Here, we elaborate how the expectation value of the spin current operator results in the quantized value even in the case where the spin is not well defined. As stated in the main text, the trace of an operator is invariant under the unitary rotation. Specifically, let us suppose the degenerate subspace, in which $\psi_{\vec{k},1}$ and $\psi_{\vec{k},2}$ are the degenerate two orthogonal state, and rotation. Specifically, let us suppose the degenerate subspace, in which $\varphi_{\vec{k},1}$ and $\varphi_{\vec{k},2}$ are denoted as the two state in which the spin $\hat{S}$ is diagonal:

$$\begin{array}{l}\hat{S}\left|\varphi_{\vec{k},\uparrow}\right\rangle = \frac{\hbar}{2}\left|\varphi_{\vec{k},\uparrow}\right\rangle, \\ \hat{S}\left|\varphi_{\vec{k},\downarrow}\right\rangle = -\frac{\hbar}{2}\left|\varphi_{\vec{k},\downarrow}\right\rangle.\end{array} \quad [4]$$

These two sets of doubly degenerate states are unitary related as

$$\begin{pmatrix}\psi_{\vec{k},1}\\ \psi_{\vec{k},2}\end{pmatrix} = \hat{U}\begin{pmatrix}\varphi_{\vec{k},\uparrow}\\ \varphi_{\vec{k},\downarrow}\end{pmatrix}, \quad [5]$$

where $\hat{U}$ is 2×2 unitary matrix. The unitarity $\left\langle\psi_{\vec{k},n}\,\middle|\,\psi_{\vec{k},m}\right\rangle = \delta_{n,m}$ requires that the matrix $\hat{U}$ should satisfy that $\hat{U}^\dagger\hat{U} = 1$.

$$\hat{U}^\dagger\hat{U} = \begin{pmatrix}U_{11}^* & U_{21}^*\\ U_{12}^* & U_{22}^*\end{pmatrix}\begin{pmatrix}U_{11} & U_{12}\\ U_{21} & U_{22}\end{pmatrix} = \begin{pmatrix}|U_{11}|^2+|U_{21}|^2 & U_{11}^*U_{12}+U_{21}^*U_{22}\\ U_{12}^*U_{11}+U_{22}^*U_{21} & |U_{12}|^2+|U_{22}|^2\end{pmatrix} = \begin{pmatrix}1 & 0\\ 0 & 1\end{pmatrix}. \quad [6]$$

The expectation value of spin velocity for two states $\psi_{\vec{k},1}$ and $\psi_{\vec{k},2}$ is written as

$$\begin{aligned}\sum_{\alpha=1}^{2}\left\langle\psi_{\vec{k},\alpha}\left|\hat{S}\hat{\vec{v}}\right|\psi_{\vec{k},\alpha}\right\rangle = \quad & \tfrac{\hbar}{2}\left(|U_{11}|^2+|U_{21}|^2\right)\left\langle\varphi_{\vec{k},1}\left|\hat{\vec{v}}\right|\varphi_{\vec{k},1}\right\rangle + \tfrac{\hbar}{2}\left(U_{11}^*U_{12}+U_{21}^*U_{22}\right)\left\langle\varphi_{\vec{k},1}\left|\hat{\vec{v}}\right|\varphi_{\vec{k},2}\right\rangle \\ & -\tfrac{\hbar}{2}\left(U_{12}^*U_{11}+U_{22}^*U_{21}\right)\left\langle\varphi_{\vec{k},2}\left|\hat{\vec{v}}\right|\varphi_{\vec{k},1}\right\rangle - \tfrac{\hbar}{2}\left(|U_{12}|^2+|U_{22}|^2\right)\left\langle\varphi_{\vec{k},2}\left|\hat{\vec{v}}\right|\varphi_{\vec{k},2}\right\rangle.\end{aligned} \quad [7]$$

Owing to the unitarity condition given in (Eq. 6), the equation should result in

$$\sum_{\alpha=1}^{2}\left\langle\psi_{\vec{k},\alpha}\left|\hat{S}\hat{\vec{v}}\right|\psi_{\vec{k},\alpha}\right\rangle = \frac{\hbar}{2}\left\langle\varphi_{\vec{k},\uparrow}\left|\hat{\vec{v}}\right|\varphi_{\vec{k},\uparrow}\right\rangle - \frac{\hbar}{2}\left\langle\varphi_{\vec{k},\downarrow}\left|\hat{\vec{v}}\right|\varphi_{\vec{k},\downarrow}\right\rangle. \quad [8]$$

Remarkably, this equation tells that the expectation of the spin-current operator is just the difference between the spin-up current and spin-down current. The equation does not depend on whether the spin is well defined or not. This formula obviously tells that, irrespective of whether the spin is fixed ($\hat{S}_z = \pm 0.5$) or varied over $\vec{k}$-points, the spin-Hall conductivity can be calculated as a summation over the Brillouin zone of the difference between the spin-up current and the spin-down current locally at $\vec{k}(t)$.

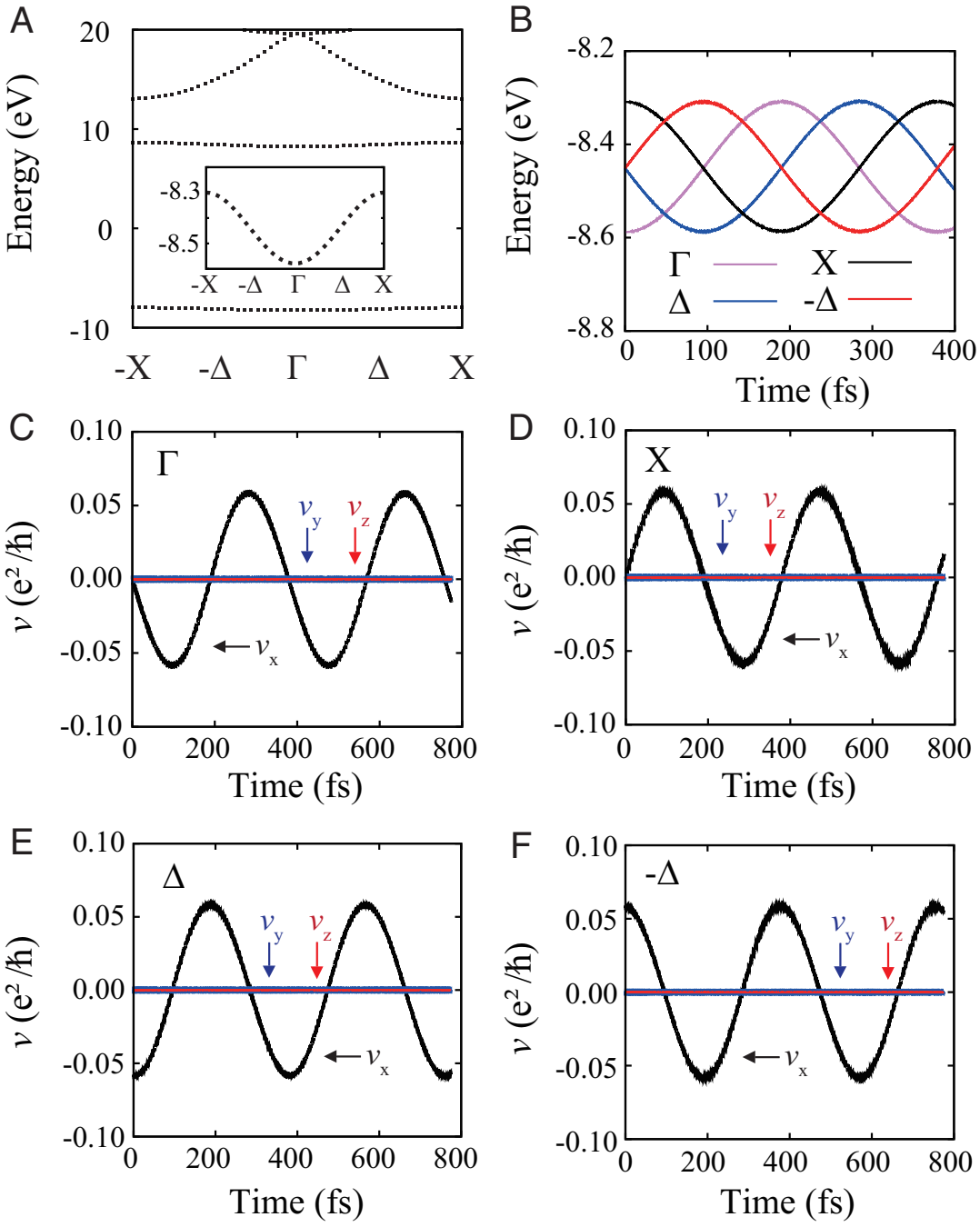

Fig. S1. Time evolution of KS states in artificial solid He. (*A*) Band structure of solid He system in the simple cubic lattice of 3Å lattice constant. (*B*) Time-variation of the band energy of the four selected states. The velocity of the Bloch state departed from (*C*) Γ, (*D*) X, (*E*) Δ, and (*F*) $-\Delta$. Inset in *A* is the valence band presented in the narrower energy window, exactly the same as in Fig. 1*A*

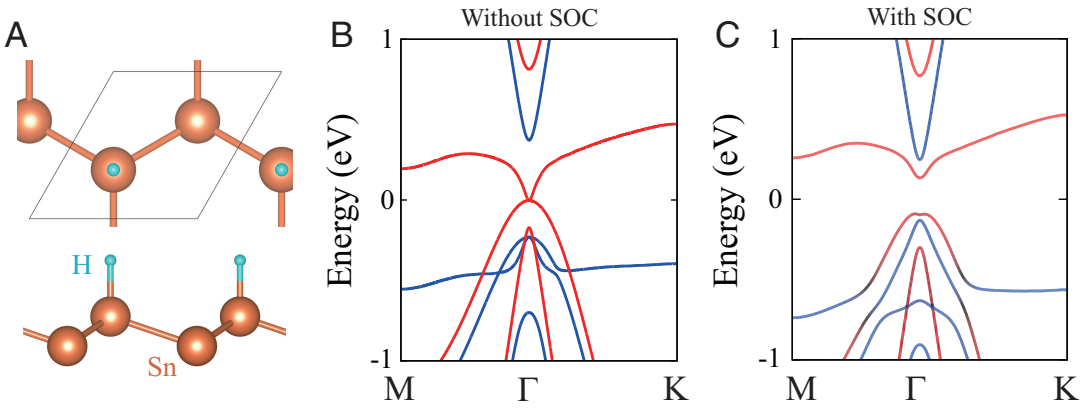

Fig. S2. Band structure of stanene with hydrogen half passivation. (*A*) schematic geometry and band structure of stanene with the half coverage of hydrogen passivation (*B*) with and (*C*) without spin orbit coupling. Red and blue indicate spin-up and spin-down states which are polarized along the out-plane direction.

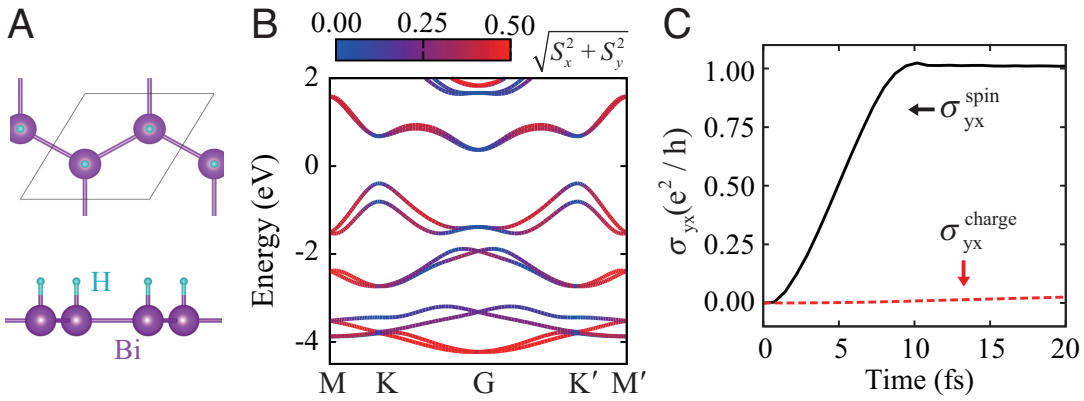

Fig. S3. QSH phase of the inversion symmetry broken Bismuthane. (*A*) Schematic geometry with the hydrogen coverage on one side. (*B*) The spin resolved band structure. (*C*) Spin and charge Hall conductivity calculated by TDDFT. In *B*, the color depicts the magnitude of the in-plane component of the spin.

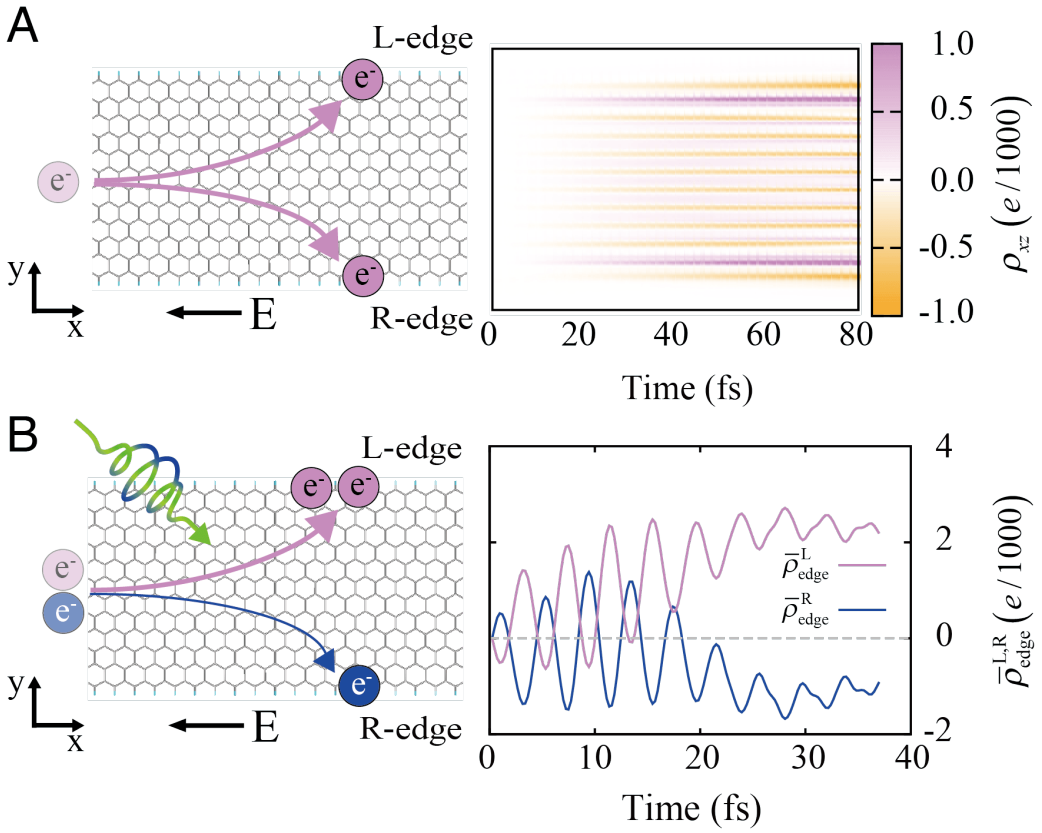

Fig. S4. Current flow in a graphene nano-ribbon biased by a static E-field. (*A*) Schematic of valley Hall effect (left) and the calculation results for the time-varying charge density. (*B*) The same as *A* but with a circularly polarized E-field in addition to the static axial bias. In *A* and *B*, the time-varying charge density is obtained by $\rho_{xz}\,(y,t) = \int\int dxdz\,[\rho(\mathbf{r},t) - \rho_0(\mathbf{r})]$, and $\bar{\rho}^{L}_{\mathrm{edge}}$ and $\bar{\rho}^{R}_{\mathrm{edge}}$ are the time-averaged charge obtained in each edge region of the ribbon ($W = 26$Å): $\bar{\rho}^{L}_{edge}(t) = \frac{1}{t}\int_0^t d\tau \int_{0.8W}^{\infty} \rho_{xz}(y,\tau)dy$ and $\bar{\rho}^{R}_{edge}(t) = \frac{1}{t}\int_0^t d\tau \int_{-\infty}^{0.2W} \rho_{xz}(y,\tau)dy$

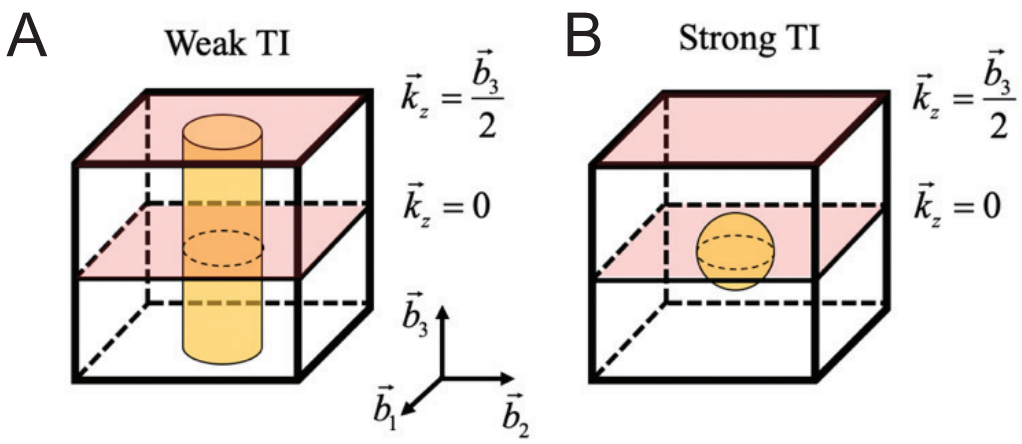

Fig. S5. Schematics of the distribution of spin Berry curvature in 3D Brillouin zone for (*A*) a weak TI and (*B*) a strong TI. The orange surface indicates the region of non-vanishing spin Berry curvature. The red square represents the two time-reversal planes of $\vec{k}_z = 0$ and $\vec{k}_z = \vec{b}_3/2$.

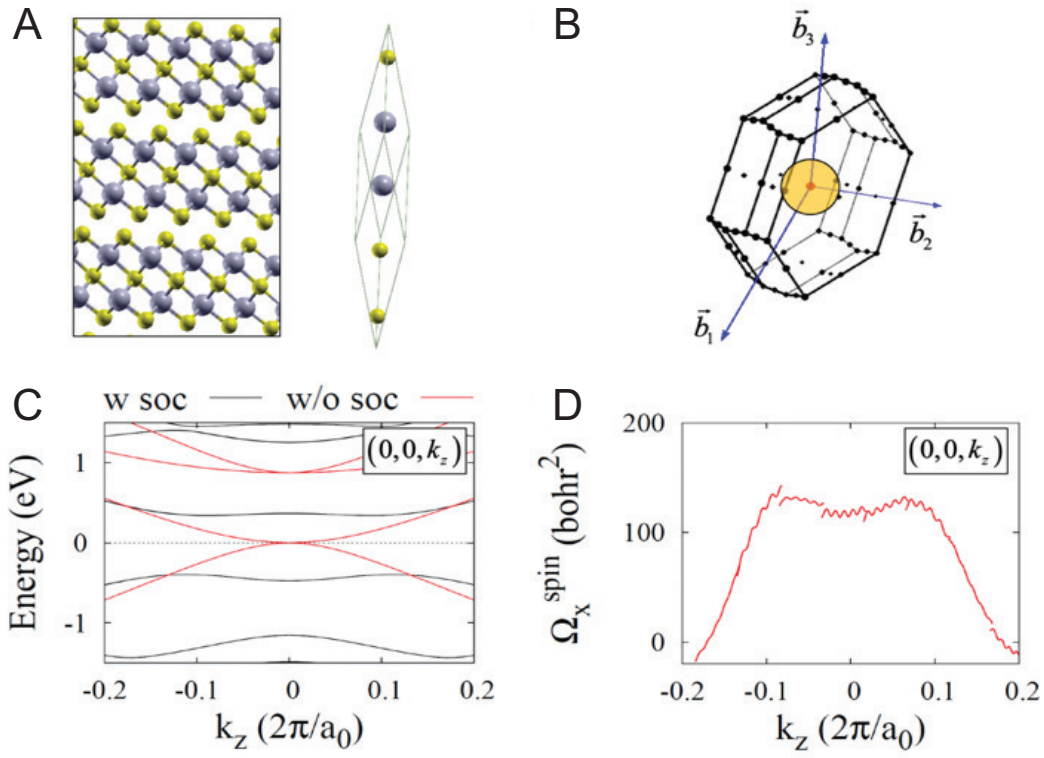

Fig. S6. (*A*) Geometry and the rhombohedral unit-cell of Bi_2Se_3. (*B*) The first Brillouin zone. (*C*) Band structure with and without SOC near the Γ point. (*D*) Spin Berry curvature along the $(0, 0, \vec{k}_z)$ direction calculated from the time-propagating Bloch states when a static E-field is applied along the z-direction. In the *B*, the orange sphere schematically depicts the region of non-vanishing spin Berry curvature.

References

1. Giannozzi P, et al. (2009) QUANTUM ESPRESSO: a modular and open-source software project for quantum simulations of materials. J. Phys-Condens. Mat. 21(39):395502.
2. Castro A, Marques MAL, Rubio A (2004) Propagators for the time-dependent Kohn-Sham equations. J. Chem. Phys. 121(8):3425-3433.
3. Andrade X, et al. (2015) Real-space grids and the Octopus code as tools for the development of new simulation approaches for electronic systems. Phys. Chem. Chem. Phys. 17(47):31371.
4. Castro A, et al. (2006) octopus: a tool for the application of time-dependent density functional theory. Phys. Status. Solidi. B 243(11):2465-2488.
5. Marques MAL, Castro A, Bertsch GF, Rubio A (2003) Octopus: a first-principles tool for excited electron-ion dynamics. Comput. Phys. Commun. 151(1):60-78.
6. Perdew JP, Burke K, Ernzerhof M (1996) Generalized gradient approximation made simple. Phys. Rev. Lett. 77(18):3865-3868.
7. Shin D, Lee G, Miyamoto Y, Park N (2016) Real-Time Propagation via Time-Dependent Density Functional Theory Plus the Hubbard U Potential for Electron-Atom Coupled Dynamics Involving Charge Transfer. J. Chem. Theory Comput. 12:201-208.
8. Meng S, Kaxiras E (2008) Real-time, local basis-set implementation of time-dependent density functional theory for excited state dynamics simulations. J. Chem. Phys. 129(5):054110.
9. Sugino O, Miyamoto Y (1999) Density-functional approach to electron dynamics: Stable simulation under a self-consistent field. Phys. Rev. B 59(4):2579-2586.
10. Bertsch GF, Iwata JI, Rubio A, Yabana K (2000) Real-space, real-time method for the dielectric function. Phys. Rev. B 62(12):7998-8002.
11. Wu SC, Shan GC, Yan BH (2014) Prediction of Near-Room-Temperature Quantum Anomalous Hall Effect on Honeycomb Materials. Phys. Rev. Lett. 113(25):256401.
12. Xiao D, Yao W, Niu Q (2007) Valley-contrasting physics in graphene: Magnetic moment and topological transport. Phys. Rev. Lett. 99(23):236809.
13. Oka T, Aoki H (2009) Photovoltaic Hall effect in graphene. Phys. Rev. B 79(8):081406(R).
14. Oka T, Aoki H (2009) Photo-induced Hall Effect in graphene-effect of boundary types. J. Phys.: Conf. Series 148:012061.
15. Sie EJ, et al. (2015) Valley-selective optical Stark effect in monolayer WS_2. Nat. Mater. 14(3):290.
16. Claassen M, Jia CJ, Moritz B, Devereaux TP (2016) All-optical materials design of chiral edge modes in transition-metal dichalcogenides. Nat. Commun. 7:13074.
17. Sentef MA, et al. (2015) Theory of Floquet band formation and local pseudospin textures in pump-probe photoemission of graphene. Nat. Commun. 6:7047.
18. Hübener H, Sentef MA, De Giovannini U, Kemper AF, Rubio A (2017) Creating stable Floquet-Weyl semimetals by laser-driving of 3D Dirac materials. Nat. Commun. 8:13940.
19. Shin D, et al. (2018) Phonon-driven spin-Floquet magneto-valleytronics in MoS_2. Nat. Commun. 9:638.
20. Hasan MZ, Kane CL (2010) Colloquium: Topological insulators. Rev. Mod. Phys. 82(4):3045.
21. Yao SY, Yan ZB, Wang Z (2017) Topological invariants of Floquet systems: General formulation, special properties, and Floquet topological defects. Phys. Rev. B 96(19):195303.
22. Chen Q, Du L, Fiete GA (2018) Floquet band structure of a semi-Dirac system. Phys. Rev. B 97(3):035422.
23. Wang ZF, Liu Z, Yang JL, Liu F (2018) Light-Induced Type-II Band Inversion and Quantum Anomalous Hall State in Monolayer FeSe. Phys. Rev. Lett. 120(15):156406.
24. Mikami T, et al. (2016) Brillouin-Wigner theory for high-frequency expansion in periodically driven systems: Application to Floquet topological insulators. Phys. Rev. B 93(14):144307.
25. Sato M, Takayoshi S, Oka T (2016) Laser-Driven Multiferroics and Ultrafast Spin Current Generation. Phys. Rev. Lett. 117(14):147202.
26. Esin I, Rudner MS, Refael G, Lindner NH (2018) Quantized transport and steady states of Floquet topological insulators. Phys. Rev. B 97(24):245401.
27. Lindner NH, Refael G, Galitski V (2011) Floquet topological insulator in semiconductor quantum wells. Nat. Phys. 7(6):490.
28. Fu L, Kane CL, Mele EJ (2007) Topological insulators in three dimensions. Phys. Rev. Lett. 98(10):106803
29. Moore JE (2013) Topological Insulators: Chapter 2. Theory of Three-Dimensional Topological Insulators (Elsevier).
30. Kane CL, Mele EJ (2005) Z(2) topological order and the quantum spin Hall effect. Phys. Rev. Lett. 95(14):146802.